The Astrophysical Journal, 873:80 (8pp), 2019 March 1 https://doi.org/10.3847/1538-4357/ab03d0

Unified Quantitative Description of Solar Wind Turbulence Intermittency in Both Inertial and Kinetic Ranges

Jiansen He[1], Ying Wang[1], and Luca Sorriso-Valvo[2,3]
[1] School of Earth And Space Sciences, Peking University, Beijing 100871, People's Republic of China; jshept@pku.edu.cn
[2] Nanotec/CNR, U.O.S. di Cosenza, Ponte P. Bucci, cubo 31C, I-87036 Rende, Italy
[3] Departamento de Fisica, Escuela Politcnica Nacional, Quito, Ecuador
Received 2018 November 30; revised 2019 January 8; accepted 2019 January 22; published 2019 March 6

Abstract

There are various ways of describing intermittent features in space plasma turbulence, but we lack a unified paradigm to connect the results from these different approaches. In this work, we aim to construct a unified paradigm to describe various intermittency-related quantities with the same set of parameters. The Castaing function, which describes the scale-dependent turbulence amplitude as a logarithmic normal distribution, is adopted as a fitting function to describe the probability distribution of magnetic field difference at various timescales τ. Two fitting parameters (μ, λ) as a function of τ are obtained and regarded as the fundamental information, based on which various characteristics related to intermittency can be derived at one time, e.g., the high-order structure functions, their scaling exponent as a function of the order, or the flatness as a function of τ. We find it is the derivative ratio, $\mathrm{DR} = \frac{d\lambda^2}{d(\ln\tau)}\Big/\frac{d\mu}{d(\ln\tau)}$, that determines the order trend of the scaling exponent $\zeta(\mathrm{m})$. A negative DR of a small absolute is responsible for a curved $\zeta(\mathrm{m})$ in the inertial range, and a large positive DR leads to a straight $\zeta(\mathrm{m})$ in the kinetic range. Therefore, it is suggested that the probability distribution function of the magnetic increments spreads in width ($\lambda(\tau)$) with decreasing τ in the inertial range, while it is saturated and even slightly reduced in the kinetic range. Moreover, it is found that the turnings between the inertial and kinetic scales for the two Castaing fitting parameters $\mu(\tau)$ and $\lambda^2(\tau)$ occur at different scales: $\ln\tau \sim 0$ and $\ln\tau \sim 2$, respectively. The reason for this different behavior is still unclear.

Key words: interplanetary medium – solar wind – turbulence

1. Introduction

Intermittency, an important aspect of turbulence, is regarded as the result of inhomogeneous cascading with a fluctuating energy transfer rate in space (Frisch 1995; Sorriso-Valvo et al. 1999; Bruno & Carbone 2013; Osman et al. 2014). The intermittent structures are locally coherent places with stronger fluctuations, where more turbulence energy is transferred, dissipated, and converted to gas kinetic energy (Wan et al. 2015; Zhang et al. 2015). In the solar wind, intermittency and waves are currently being considered as two possible populations of turbulence, through which turbulence energy is channeled down to particle kinetic scales (Wang et al. 2013; He et al. 2015a, 2015b; Howes 2015, 2017; Klein 2017; Jiansen et al. 2018). Current sheets probably involving magnetic reconnection are one kind of coherent magnetic structure (Gosling et al. 2005; Phan et al. 2006; Borovsky 2008; Li et al. 2011; Servidio et al. 2011; Pulupa et al. 2014). Multi-order structure functions (SFs) at kinetic scales inside and outside the reconnection exhaust exhibit different behaviors: multifractal and monofractal scalings for the former and latter, respectively (Wang et al. 2015). There are several methods to identify the intermittent structures: "partial variance increment" analysis of the difference sequences at various time lags (Greco et al. 2009); "local intermittency measure" based on local wavelet coefficients as normalized to the global averaged value (Bruno et al. 2001); "local energy transfer" based on the third-order moment scaling law (Sorriso-Valvo et al. 2018). Magnetic reconnection sites and vast exhaust regions as coherent structures in the solar wind are found to be bounded by a pair of compound discontinuities and emit significant Alfvénic waves due to firehose instability, thereby building up a complicated set of intermittency (Liu et al. 2012; Jiansen et al. 2018). However, magnetic reconnection configuration is not a unique type of intermittent structure, which can also be of other types, e.g., rotational discontinuities, tangential discontinuities with unidirectional magnetic field, local large-amplitude waves (Greco & Perri 2014; Zhang et al. 2015; Yang et al. 2017). The introduction of kinetic-scale intermittent structures of different dimensions, e.g., sheet-type or tube-type, is suggested to modify the spectral index of power spectral densities (PSDs)($k_\perp$), adjust the critical-balance relation between $k_\perp$ and $k_\parallel$, and probably increase the frequency ω (Zhao et al. 2016).

Intermittency also has statistical influence on the turbulence characteristics. The simplified model of turbulence without intermittency is characterized with the following classical features (Tu et al. 1996). (1) The probability distribution function (PDF) of field increments can be approximated with a Gaussian distribution ($\mathrm{PDF}(\delta B(\tau)) \sim N(0,\ \sigma^2(\tau))$). (2) The flatness of $\mathrm{PDF}(\delta B(\tau))$ stays around 3, a characteristic value pertaining to a Gaussian distribution. (3) The SF of order m (SF (τ; m)) can be described by a power-law function with the exponent being linearly scaled ($\mathrm{SF}(\tau; m) \sim \tau^{\zeta(m)} \sim \tau^{\alpha_m}$). However, the actual turbulence cannot be fully described without including the effects of intermittency. Due to the existence of intermittency, $\mathrm{PDF}(\delta B(\tau))$ deviates from the Gaussian distribution, with a remarkable extended tail on the end of both wings. Furthermore, $\mathrm{PDF}(\delta B(\tau))$ can be super-Gaussian at the center, sub-Gaussian at the intermediate range, and super-Gaussian at the distant tail. The flatness rises from the level of 3 as the scale τ decreases from large values in the MHD inertial range (Pei et al. 2016). However, the increase of flatness slows down, ceases, and even turns to a decrease when coming to the kinetic scales (Wu et al. 2013). The scaling

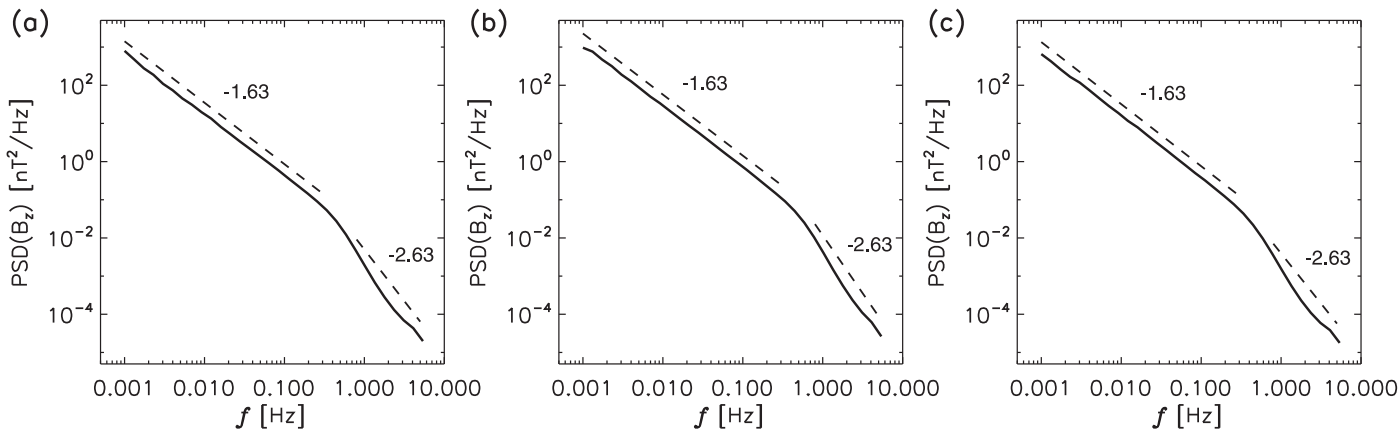

Figure 1. Power spectral density of B_z fluctuations in the three time intervals. The MHD inertial range with a spectral index of about -1.63 can be found at $f < 0.3$ Hz. In the kinetic range beyond the spectral break, the PSD profile is steeper, with its spectral index being even smaller than -2.63. The tiny bump of PSD at the highest frequency end may be due to an aliasing effect caused by a finite sampling frequency.

exponent ζ(m) behaves differently in the inertial and kinetic ranges: a concave curve in the inertial range and a nearly straight line in the kinetic range (Kiyani et al. 2009).

To quantitatively describe the statistical characteristics of intermittency, one needs to invoke a mathematical model that can account for the features of various aspects as completely as possible. There have been various mathematical models dedicated to explaining the performance of ζ(m) by assuming the fragmentation of energy transfer rate. In the random-β model, the energy transfer fragmentation is defined by a random space-filling factor variable β, which is assumed to be a bimodal distribution with a probability of ξ for space-filling eddies and a rest probability of 1-ξ for planar sheets (Benzi et al. 1984). In the p-model, the energy fragmentation bipartitions unequally over two equally-partitioned spatial intervals (Meneveau 1991; Carbone 1993). In the log-Poisson model, the turbulence amplitude decays over scales by a factor of β^q, where β is a quantity less than 1 and q is a random variable following a Poisson distribution (She & Leveque 1994; Chandran et al. 2015). The above three models based on the idea of energy transfer rate fragmentation help us to understand the essence of intermittency by comparing observational and modeled ζ(m).

On the other hand, the observational PDF(δB(τ)) has hereto been scarcely reproduced or compared with models of energy transfer rate fragmentation. The profile of PDF(δB(τ)) cannot be simply fitted with a Gaussian function, since the amplitude of δB(τ), $\sigma(\tau)$, may be widely distributed rather than a certain fixed value. If $\sigma(\tau)$ is log-normally distributed as $\ln(\sigma(\tau)) \sim N(\mu(\tau), \lambda^2(\tau))$ and δB(τ) is normally distributed as $\delta B(\tau) \sim N(0, \sigma^2(\tau))$, then the function to describe the PDF(δB(τ)) is the so-called Castaing function (Castaing et al. 1990). The Castaing function has been successfully employed to fit and describe the features of PDF for solar wind turbulent disturbance (Sorriso-Valvo et al. 1999, 2015; Luo et al. 2011; Ragot 2013).

By invoking the Castaing function, the intermittent turbulence can be approximately represented with two scale-dependent parameters ($\mu(\tau)$, $\lambda^2(\tau)$). How are these two scale-dependent parameters related with the other frequently used measures of intermittency, e.g., flatness ($F(\tau)$), scaling exponent (ζ(m)), and so on? What physics can be implied from the different scaling properties of $\mu(\tau)$, $\lambda^2(\tau)$ in the inertial range and in the kinetic range? These questions are about to be addressed in this work.

2. Formulas of SF, Flatness, and Scaling Exponent Derived from Castaing Function

As one of the possible PDFs of turbulent fluctuation δB(τ) at scale τ, the Castaing function uses a log-normal distribution for the fluctuation standard deviation $\sigma(\tau)$ and a normal distribution for δB (τ) belonging to a subset with a certain $\sigma(\tau)$. The PDF of δB is an integral of joint PDF, PDF(δB, ln σ), over the range of variable lnσ:

$$\begin{aligned}\mathrm{PDF}(\delta B) &= \int_{-\infty}^{+\infty} \mathrm{PDF}(\delta B, \ln\sigma) d\ln\sigma \\ &= \int_{-\infty}^{+\infty} \mathrm{PDF}(\delta B|\ln\sigma)\cdot \mathrm{PDF}(\ln\sigma) d\ln\sigma, \end{aligned} \quad (1)$$

where the joint PDF, PDF(δB, ln σ), is a multiplication of conditional PDF, $PDF(\delta B|\ln\sigma)$, and PDF(ln σ). Therefore, the final format of PDF(δB) can be written as

$$\begin{aligned}&\mathrm{PDF}_{\mathrm{Castaing}}(\delta B) \\ &= \int_{-\infty}^{+\infty} \frac{1}{\sqrt{2\pi}\sigma} \\ &\quad \times \exp\left(\frac{-\delta B^2}{2\sigma^2}\right)\frac{1}{\sqrt{2\pi}\lambda}\exp\left(\frac{-(\ln\sigma-\mu)^2}{2\lambda^2}\right) d\ln\sigma. \end{aligned} \quad (2)$$

The SF of m-order, SF_m, is defined as

$$\mathrm{SF}_m(\tau) = \frac{1}{T}\int_0^T |\delta B(t;\tau)|^m dt. \quad (3)$$

The SF can also be expressed as

$$\mathrm{SF}_m(\tau) = \int_{-\infty}^{+\infty} |\delta B|^m \mathrm{PDF}_{\mathrm{Castaing}}(\delta B;\mu(\tau),\lambda^2(\tau)) d\delta B. \quad (4)$$

It can be seen that $\mathrm{SF}_m(\tau)$ is a two-fold integral, the integration order of which needs to be switched in order to have an analytic integration result. As a consequence, $\mathrm{SF}_m(\tau)$ can be described directly by $\mu(\tau)$ and $\lambda^2(\tau)$ as

$$\mathrm{SF}_m(\tau) = C(m)\exp\left(\frac{m^2}{2}\lambda^2(\tau) + m\mu(\tau)\right), \quad (5)$$

where $C(m) = \frac{\sqrt{2}^m}{\sqrt{\pi}}\Gamma\left(\frac{1+m}{2}\right)$. Based on the formula of $\mathrm{SF}_m(\tau)$, the flatness can be expressed directly by $\lambda^2(\tau)$ as well

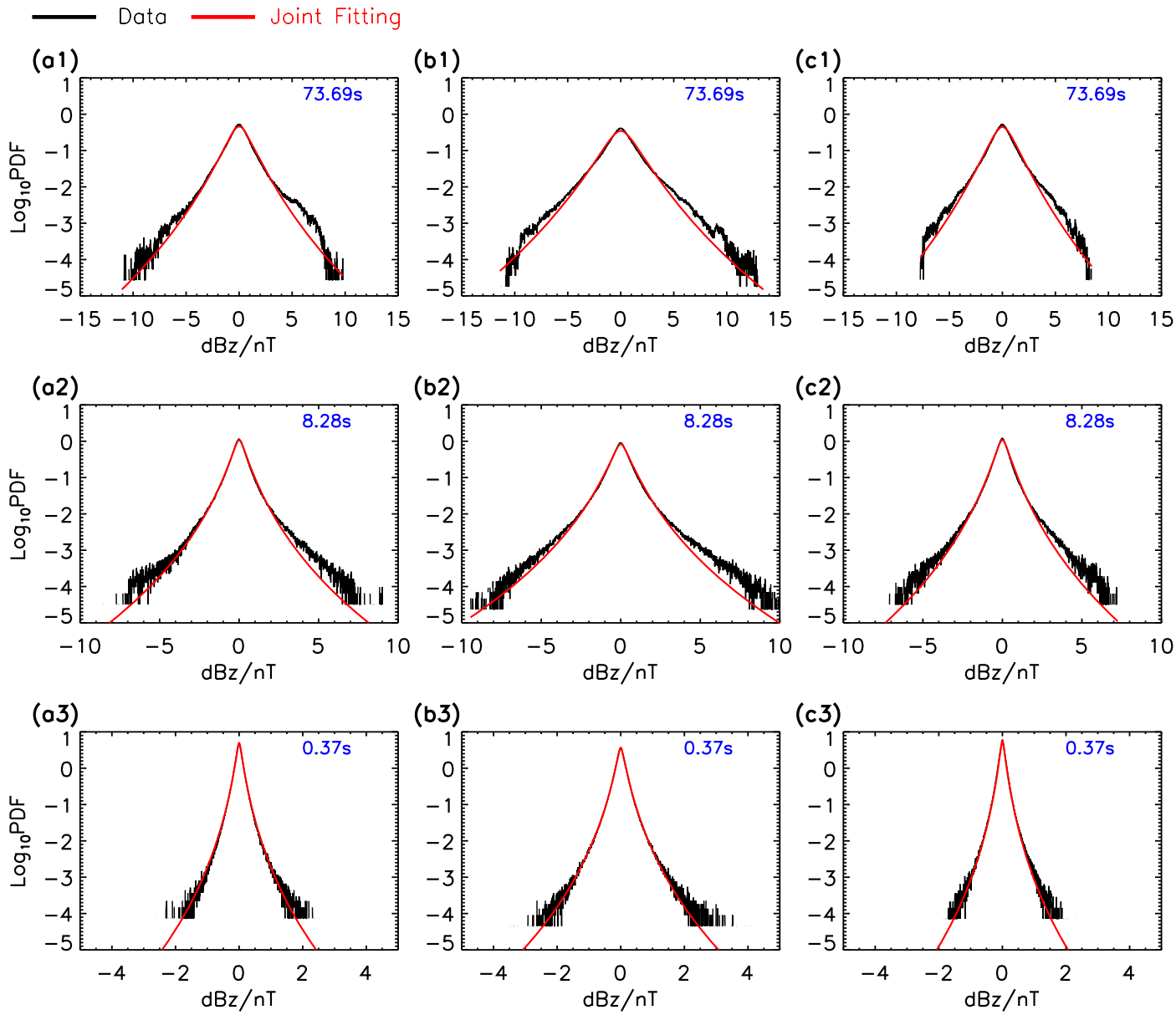

Figure 2. PDFs of dB_z in logarithmic scale at three different time lags (from top to bottom) of three cases (from left to right). The black and red lines respectively represent the original PDFs and fitted PDFs, a joint fitting result of PDF(dB_z; $\mu(\tau)$, $\lambda^2(\tau)$) and SF(m; $\mu(\tau)$, $\lambda^2(\tau)$) based on Castaing function.

(Sorriso-Valvo et al. 2015):

$$F(\tau) = \frac{\mathrm{SF}_4(\tau)}{\mathrm{SF}_2^2(\tau)} = 3\exp(4\lambda^2(\tau)). \tag{6}$$

The scaling exponent $\zeta(m)$ for $\mathrm{SF}_m(\tau)\tau^{\zeta(m)}$ is therefore determined by the scale dependence of $\mu(\tau)$ and $\lambda^2(\tau)$,

$$\zeta(m) = \frac{d(\ln \mathrm{SF}_m)}{d\ln\tau} = \frac{m^2}{2}\frac{d\lambda^2}{d\ln\tau} + m\frac{d\mu}{d\ln\tau}. \tag{7}$$

3. Fitting Procedure under the Castaing Framework

According to our test experience of the solar wind magnetic turbulence, we find that PDF(δB|λ, μ) and SF(m|λ, μ) have different sensitivities to the two fitting parameters (λ, μ) of the Castaing function, although both PDF(δB|λ, μ) and SF(m|λ, μ) are determined by both $\lambda(\tau)$ and $\mu(\tau)$. PDF(δB(τ)) seems more sensitive to $\lambda(\tau)$, while SF(τ; m) is more sensitive to $\mu(\tau)$. Therefore, we suggest conducting a simultaneous fitting analysis of PDF(δB(τ)) and SF(τ; m), in order to more precisely estimate the fitting parameters ($\lambda(\tau)$, $\mu(\tau)$). We utilize the "Gradient Descent Algorithm" to approach the minimum level of a joint residual, and thereby find out the parameters (λ, μ), possessing the best-fitting results of both PDF(δB|λ, μ) and ln(SF(m|λ, μ)). The joint residual is defined as the weighted sum of residuals between fitting results and observational data, which reads as

$$\sigma_{\mathrm{joint}} = k_1\sigma_{\mathrm{PDF}} + k_2\sigma_{\mathrm{lnSF}}, \tag{8}$$

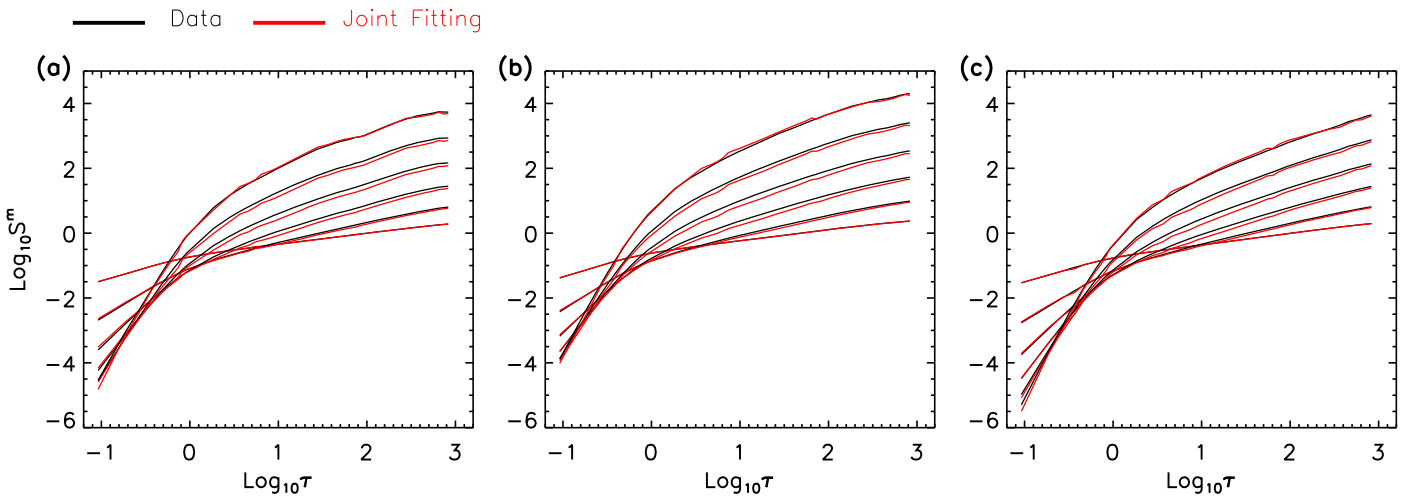

Figure 3. Relation between $lg_{10}(\mathrm{SF}(\tau; m))$ and $lg_{10}(\tau)$. The structure functions calculated directly from data are plotted in black, while their counterparts, as obtained from a joint fitting result of $\mathrm{SF}(m; \mu(\tau), \lambda^2(\tau))$ and $\mathrm{PDF}(dB_z; \mu(\tau), \lambda^2(\tau))$, are plotted in red.

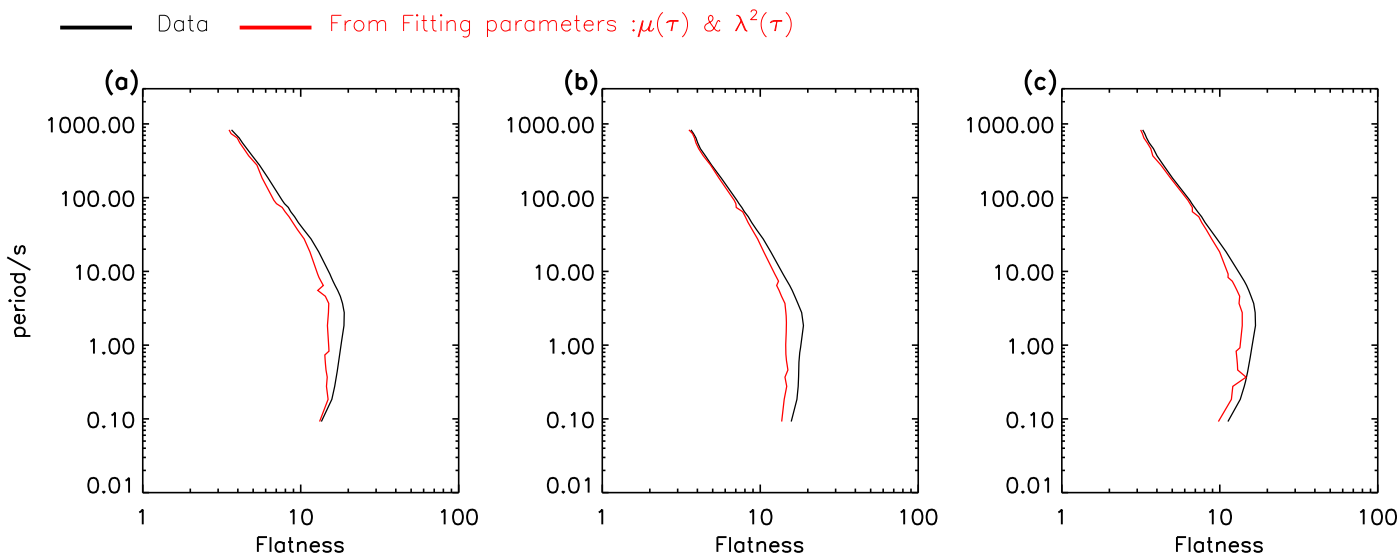

Figure 4. Scale dependence of flatness ($F(\tau)$) for three cases (from left to right). The black lines are plotted with $F(\tau) = \frac{\langle dB_z(t;\tau)^4\rangle}{\langle dB_z(t;\tau)^2\rangle^2}$. The red lines are plotted on the basis of $F(\tau) = 3e^{4\lambda^2}$, with $\lambda^2(\tau)$ being the fitting parameter of the Castaing function for $PDFs(dB_z)$ at time lag τ.

where k_1 and k_2 are weights set to be 0.5 and 0.5 in this work. The residuals σ_{PDF} and $\sigma_{\ln \mathrm{SF}}$ are calculated as

$$\begin{cases} \sigma_{\mathrm{PDF}}(\lambda, \mu) = \sum_i (\mathrm{PDF}_{\mathrm{fit}}(\delta B_j|\lambda, \mu) - \mathrm{PDF}_{\mathrm{data}}(\delta B_j))^2 \\ \sigma_{\ln\mathrm{SF}}(\lambda, \mu) = \sum_m (\ln \mathrm{SF}_{\mathrm{fit}}(m|\lambda, \mu) - \ln \mathrm{SF}_{\mathrm{data}}(m))^2 \end{cases}. \quad (9)$$

It can be seen that $\sigma_{\mathrm{joint}}(\lambda, \mu)$ is a two-dimensional parameter space function, hence the position of the minimum $\sigma_{\mathrm{joint}}(\lambda, \mu)$ can be obtained with the "Gradient Descent Algorithm." At each iteration, (λ, μ) are updated as

$$\begin{cases} \lambda_{i+1} = \lambda_i + (-l_\lambda)\frac{\partial\sigma}{\partial\lambda}\Big|_{\lambda=\lambda_i} \\ \mu_{i+1} = \mu_i + (-l_\mu)\frac{\partial\sigma}{\partial\mu}\Big|_{\mu=\mu_i} \end{cases}, \quad (10)$$

where l is the step length.

4. Fitting of Observational PDF and SF

We apply the aforementioned fitting procedure to three samples of fast solar wind measurements from the *WIND* spacecraft during the time intervals [1995 April 8, 1995 April 12], [1995 May 3, 1995 May 8], and [2008 March 10, 2008 March 15], respectively. Before conducting the fitting process, we plot in Figure 1 the PSDs of $\boldsymbol{B}_z$-component fluctuations for the three cases. The inertial and kinetic ranges can be clearly identified according to their different power-law characteristics. We know that the background interplanetary magnetic field (IMF) lines usually lie within the x–y plane of the GSE coordinates when measured by the *WIND* spacecraft in the ecliptic plane. The turbulence of fast solar wind is characterized with Alfvénic fluctuations, which oscillate transversely to the background IMF direction. Therefore, $\boldsymbol{B}_z$ fluctuation, as compared to $\boldsymbol{B}_x$ and $\boldsymbol{B}_y$, is a component more appropriate to represent the turbulent fluctuations.

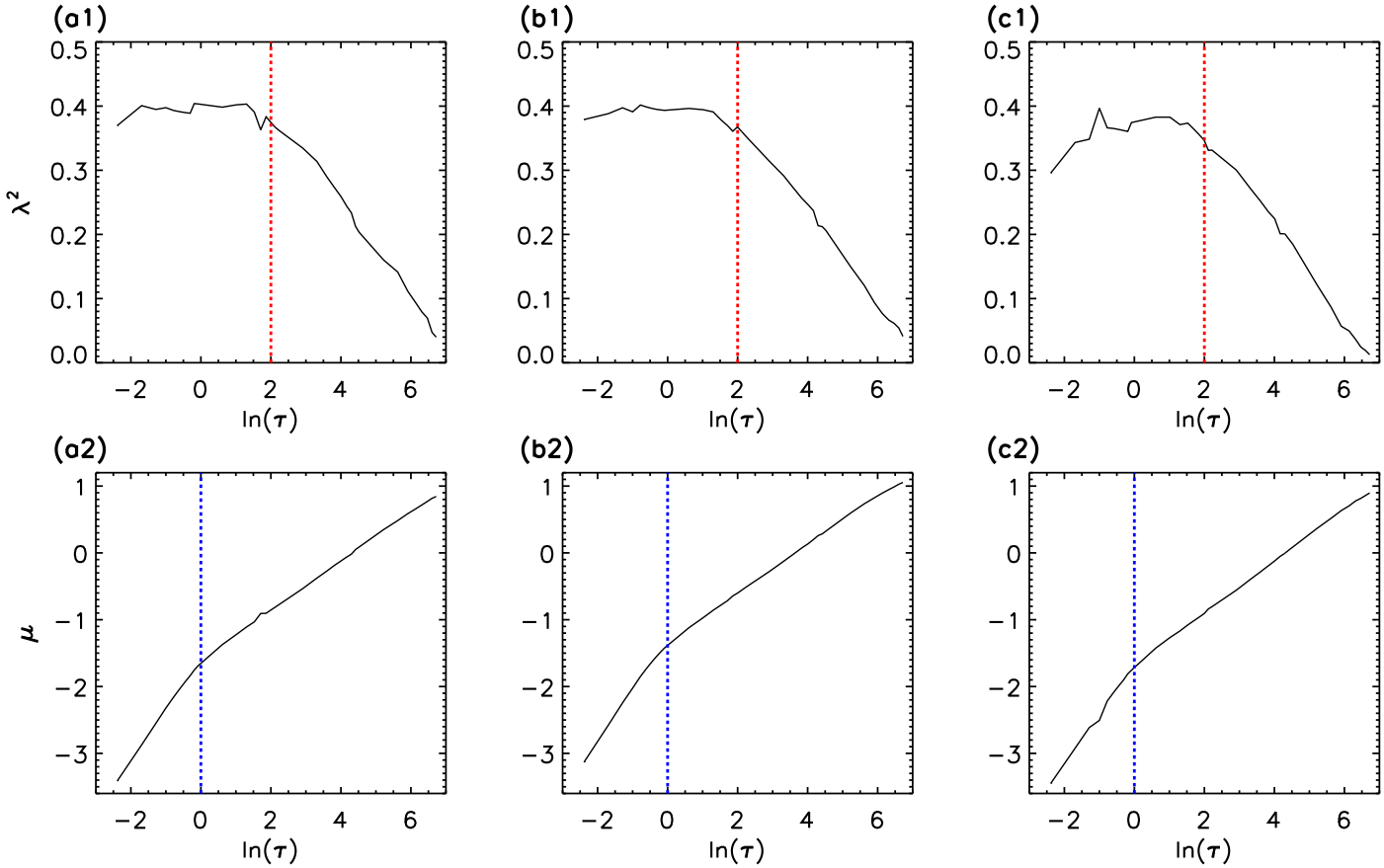

Figure 5. Scale dependence of μ and λ^2 for three cases (from left to right). The profile transitions (break) of μ and λ^2 happen at $\ln\tau_0$ and $\ln\tau_2$, respectively.

The time difference of B_z at different time lags τ is calculated as

$$dB_z(t;\tau) = B_z\left(t + \frac{\tau}{2}\right) - B_z\left(t - \frac{\tau}{2}\right). \quad (11)$$

PDFs of dB_z at different time lags of τ are constructed, and displayed as black lines in Figure 2. The fitted profiles, $\mathrm{PDF_{fit}}(dB_z;\ \lambda,\ \mu)$, are also plotted as red lines in Figure 2. The panels from top to bottom rows in Figure 2 correspond to three different time lags: $\tau_1 \sim 73.69$ s, $\tau_2 \sim 8.28$ s, and $\tau_3 \sim 0.37$ s. It can be seen that the fitting results match with the observational data at all investigated scales of τ, suggesting the successful application of the fitting procedure. The three time lags (τ_1, τ_2, and τ_3) we choose in our study are representatives of three characteristic scales: (1) the scale well in the MHD inertial range; (2) the scale near the end of MHD regime but not yet reaching the spectral break; (3) the scale beyond the break and near the onset of the kinetic range.

The fitting matches better as the scale becomes smaller. It is found that PDF's profile appears slightly asymmetric in the inertial range, with a tiny enhancement on the right wing, while transits to symmetry are at scales in the "dissipative" range. This phenomenon of a transition from asymmetry toward symmetry indicates the reduction of net energy transfer rate (cascading rate) when moving from the inertial range into the dissipation range, and is a direct consequence of the third-order moment scaling law that defines intermittency in turbulence (Politano & Pouquet 1998). Therefore, the symmetric Castaing fitting function used in this work may be more appropriate to describe the PDF in the dissipation range and the higher-frequency part of the inertial range, as compared to that in the lower-frequency part of inertial range.

The multi-order SF, $\mathrm{SF}(\tau;\ m)$, is another object to be fitted with the fitting procedure. The black curves in the three panels of Figure 3 represent the three cases of SFs with the order increasing from $m = 0.5$ to $m = 3$, for which statistical convergence is safely verified. As a comparison, the fitting results of $\mathrm{SF}(m|\lambda(\tau),\ \mu(\tau))$ are plotted as red curves. It can be seen that the observational SF is fitted very well. According to the standard analysis, the $\mathrm{SF}(\tau;\ m)$ are fitted as a function of τ for every individual order m. In the present work, $\mathrm{SF}(m|\lambda(\tau),\ \mu(\tau))$ is fitted as a function of m at every scale of τ. The advantage of the present fitting method over the former ones lies in the self-consistent incorporation of two objects (PDF and SF) to be fitted self-consistently in one single procedure. To our knowledge, this is the first successful attempt to fit the whole set of SF based on the derivation of the Castaing function.

The third product of the fitting procedure will be the scale-dependent profile of the flatness ($\mathrm{F}(\tau)$). Figure 4 displays a comparison between observed and fitting-derived flatness profiles, both of which illustrate an analogous trend: a linear increase in the log–log scale at large scales (indicating the predicted power-law increase), saturation at intermediate scales, and finally a weak decrease at small scales, below the MHD range. The fitting-derived flatness is slightly smaller than the observed counterpart, which may be related to the fitting defect on the PDF's tail, as illustrated in Figure 1.

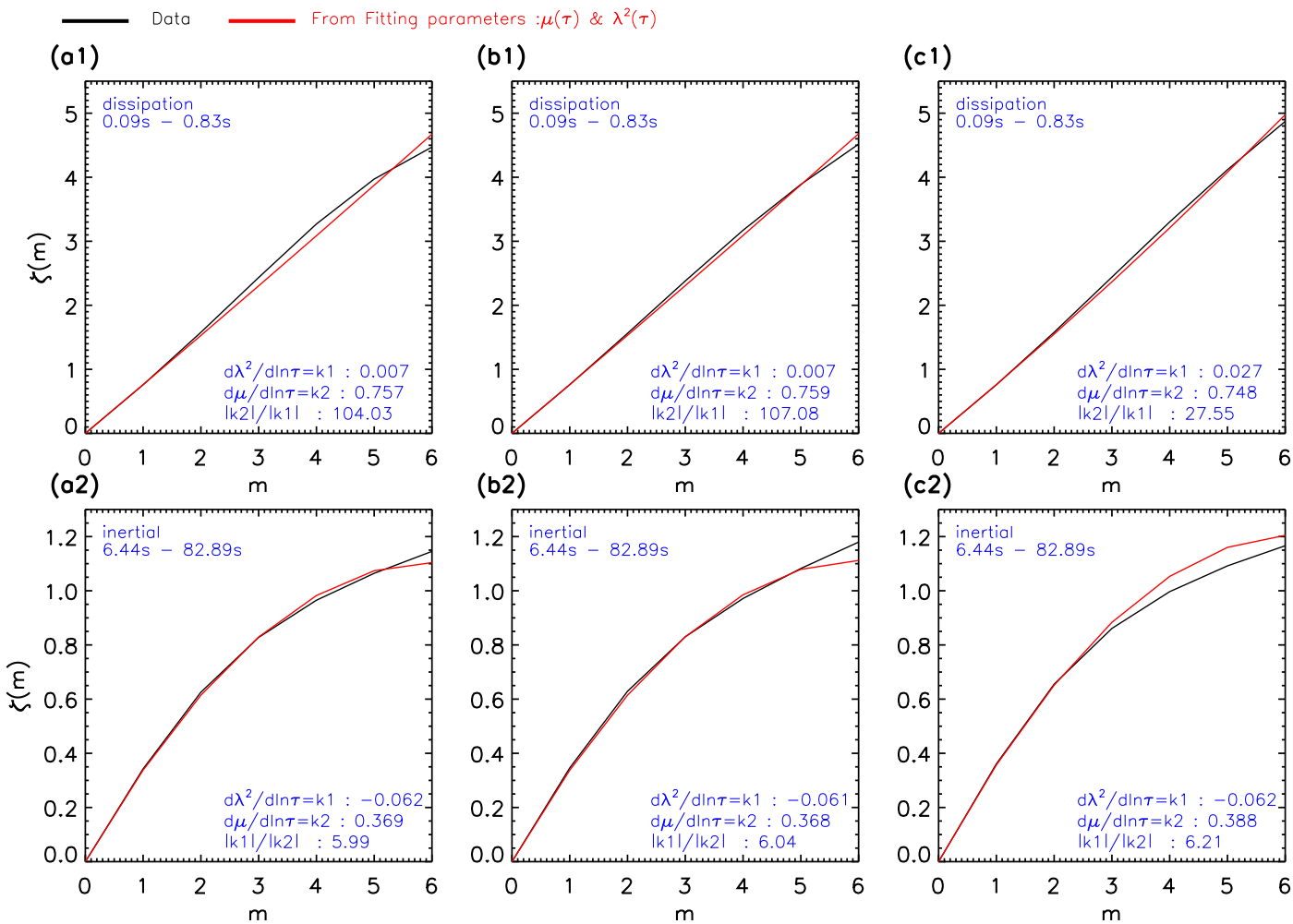

Figure 6. Scaling exponent of structure function vs. the order m in both the kinetic range (top) and MHD range (bottom). The $\zeta(m)$ values on the black lines are obtained from direct fitting of data with $\mathrm{SF}(\tau; m) \sim \tau^{\zeta(m)}$, while the $\zeta(m)$ values on the red lines are calculated with $\zeta(m) = \frac{d(\ln S_m)}{d(\ln \tau)} = \frac{m^2}{2}\frac{d\lambda^2}{d(\ln \tau)} + m\frac{d\mu}{d(\ln \tau)}$, where $\mu(\tau)$ and $\lambda^2(\tau)$ are fitting parameters of the Castaing function for PDFs(dB_z) at various time lags τ. The straightness of $\zeta(m)$ in the kinetic range is caused by a relatively larger $\left|\frac{d\lambda^2}{d(\ln \tau)}\right| \Big/ \left|\frac{d\mu}{d(\ln \tau)}\right|$, while the curvature of $\zeta(m)$ in the MHD range is due to a relatively smaller $\left|\frac{d\lambda^2}{d(\ln \tau)}\right| \Big/ \left|\frac{d\mu}{d(\ln \tau)}\right|$ and negative $\frac{d\lambda^2}{d(\ln \tau)}$.

Table 1
Analysis of Controlling Parameters Responsible for the Multifractal and Monofractal Scalings of Magnetic Turbulence in the Respective Inertial and Dissipation Ranges

	Variables, Functions	Case-1	Case-2	Case-3
Inertial Range ($t \sim$ [6.44, 82.89 s]) (Multifractal Scaling)	$d/d\ln\tau$	0.368	0.374	0.386
	$d\lambda^{22}/d\ln\tau$	−0.059	−0.062	−0.066
	$\lvert d/d\ln\tau\rvert/\lvert d\lambda^{22}/d\ln\tau\rvert$	6.22	6.01	5.87
	ζ(m)	concave	concave	concave
Dissipation Range ($t \sim$ [0.09, 0.83 s]) (Monofractal Scaling)	$d/d\ln\tau$	0.756	0.756	0.743
	$d\lambda^2/d\ln\tau$	0.007	0.004	0.027
	$\lvert d/d\ln\tau\rvert/\lvert d\lambda^2/d\ln\tau\rvert$	116.17	193.77	27.34
	ζ(m)	linear	linear	linear

5. Scale Dependences of $\mu(\tau)$ and $\lambda^2(\tau)$ and Their Influence on the Fractal Scaling Behavior

Figure 5 displays the profiles of the fitting parameters (μ, λ^2) over time lags τ. The value of $\mu \sim \langle \ln \sigma \rangle$ decreases monotonically with decreasing τ, illustrating two different power laws (linear scaling in the log–log plot) separated by a break located at $\langle \ln \sigma \rangle \sim 0$. This can be expressed as

$$\mu \sim \langle \ln \sigma \rangle \sim \alpha_\mu \ln \tau, \begin{cases} \alpha_\mu \sim 0.4, \ln \tau > 0 \\ \alpha_\mu \sim 0.7, \ln \tau < 0 \end{cases}. \quad (12)$$

Similarly, λ^2 first increases, then saturates, and finally slightly decreases, as the scale τ reduces from larger than 400 s down to

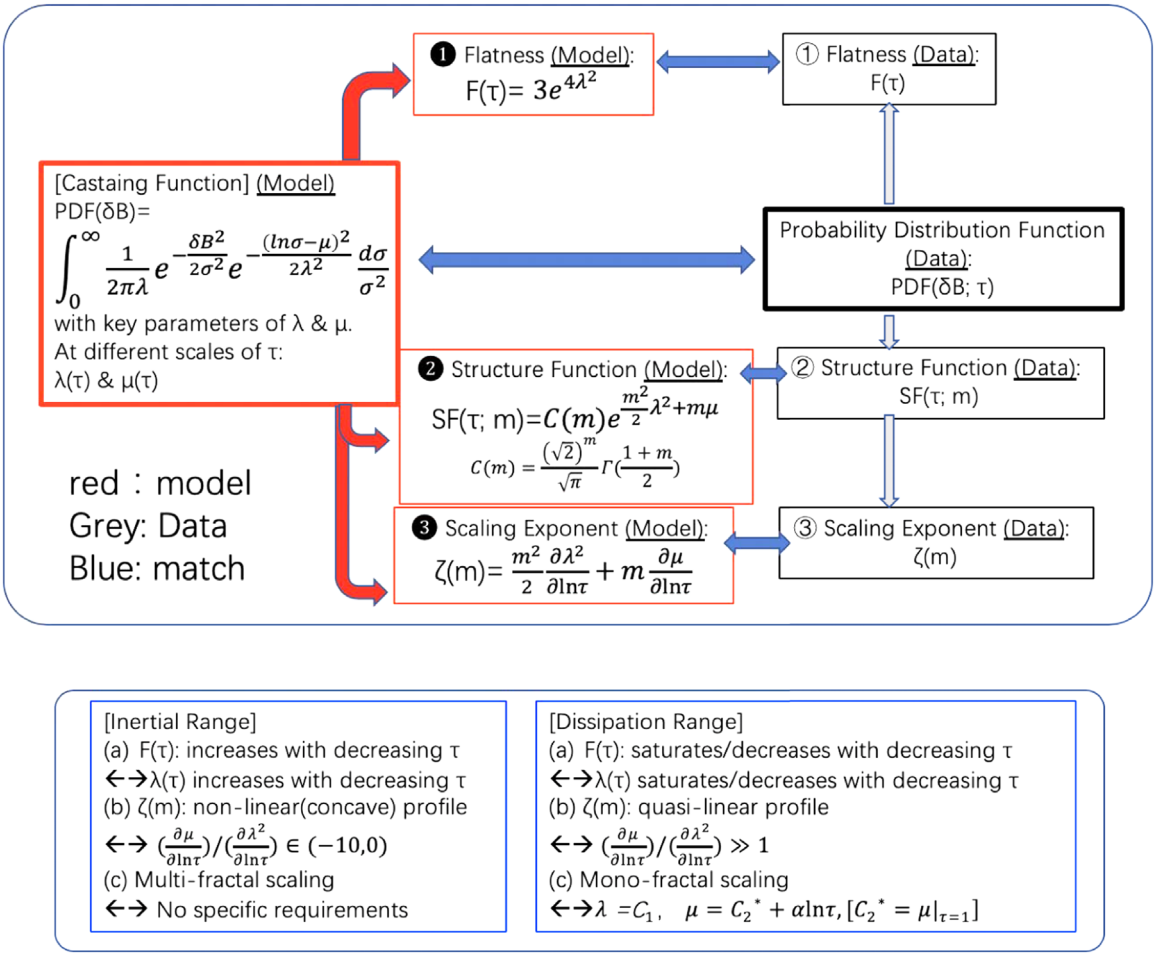

Figure 7. Sketch of the modeling framework (highlighted with red boxes and red arrows) as derived and extended from the Castaing function. The black boxes contain four functions (PDFs, flatness, structure function, scaling exponent) that are calculated directly from data. The consistency between the modeling results (red boxes) and data reductions (black boxes), as demonstrated in aforementioned figures and sections, is marked with blue bidirectional arrows. The features of flatness, scaling exponent, and fractal scaling as determined by $\mu(\tau)$ and $\lambda^2(\tau)$ in both the inertial and dissipation ranges are summarized in blue boxes.

smaller than 0.15 s. The profile of $\lambda^2(\tau)$ can be approximated as

$$\lambda^2 \sim \langle(\ln\sigma)^2\rangle \sim \alpha_\lambda \ln\tau, \begin{cases}\alpha_\lambda \sim -0.06, \ln\tau > 2\\ \alpha_\lambda \sim 0.0, \ln\tau < 0\end{cases}. \quad (13)$$

Substituting the approximations of $\mu(\tau)$ and $\lambda^2(\tau)$ into the expression of SF(τ; $m = 2$), we can get the joint scaling exponents for the second-order SF in both the inertial and dissipation range,

$$\ln \mathrm{SF}(\tau; m) = \ln C(m) + \frac{m^2}{2}\lambda^2(\tau) + m\mu(\tau) \sim \alpha_{\mathrm{SF}} \ln\tau, \begin{cases}\alpha_{\mathrm{SF}} \sim 0.68, \ \ln\tau > 2\\ \alpha_{\mathrm{SF}} \sim 1.4, \ \ln\tau < 0\end{cases}. \quad (14)$$

The scaling exponents of the second-order SF are consistent with the typical Kolmogorov power spectral density exponent $\sim -5/3$, corresponding to $-(\alpha + 1)$. The range $\ln\tau \in [0, 2]$ may be called a transition range, bridging the inertial and dissipation ranges.

The scaling exponent ζ(m) of an m-order SF with τ as the base is expressed as in Equation (7). Whether the intermittency is characterized by monofractal or multifractal scaling can be judged from the linear or nonlinear profile of ζ(m). At different τ, the profile of ζ(m) can be different, e.g., changing from a nonlinear to a linear trend with decreasing τ. Figure 6 displays ζ(m) at small τ in the dissipation range (upper panels), and at large τ in the inertial range (lower panels). The black lines represent the scaling exponent as estimated from the observed SF(τ, m), and the red lines represent the scaling exponent calculated from fitting parameters $\mu(\tau)$ and $\lambda^2(\tau)$ according to Equation (7). The quasi-linear trend of ζ(m) in the dissipation range, a signature of monofractal scaling of intermittency, is attributed by the large ratio of $\frac{d\lambda^2}{d(\ln\tau)}$ to $\frac{d\mu}{d(\ln\tau)}$ (e.g., $|\frac{\frac{d\lambda^2}{d(\ln\tau)}}{\frac{d\mu}{d(\ln\tau)}}| > 20$). On the contrary, the concave nonlinear trend of ζ(m) associated with the nature of multifractal scaling is mathematically determined by the small ratio ($|\frac{\frac{d\lambda^2}{d(\ln\tau)}}{\frac{d\mu}{d(\ln\tau)}}|<10$) and negative value of $\frac{d\lambda^2}{d(\ln\tau)}$.

Associated with Figure 6, Table 1 shows the values of $\frac{d\mu}{d(\ln\tau)}$, $\frac{d\lambda^2}{d(\ln\tau)}$, $|\frac{\frac{d\lambda^2}{d(\ln\tau)}}{\frac{d\mu}{d(\ln\tau)}}|$, and the inferred profile type of ζ(m) for both the inertial and dissipation ranges of the three cases. The value of $\frac{d\mu}{d(\ln\tau)}$ in the inertial range is positive and about half of that in the dissipation range. The value of $\frac{d\lambda^2}{d(\ln\tau)}$ in the inertial range is negative, while its counterpart in the dissipation range is

positive and smaller in absolute value. The characteristics of $\frac{d\lambda^2}{d(\ln\tau)}$ in both inertial and dissipation ranges are responsible for the feature of the flatness profile over the timescale, which increases to a peak around the break and then slightly reduces beyond the break. From the table, one can clearly understand the reason why the inertial and dissipation ranges have different scaling behaviors.

6. Summary and Discussion

Fitting the PDFs of turbulent field increments at various scales with a Castaing function has been adopted here as an efficient approach to comprehensively quantify the statistics feature of turbulence. Quantitative expressions based on the fitting parameters are obtained to describe the scale dependence of multi-order SFs (SF(τ; m)), the fractal scaling behavior (order dependence) of the scaling exponent of SFs (ζ(m)), and the scale dependence of flatness (F(τ)). The full functions of procedure are summarized in Figure 7. The scale dependences of fitting parameters ($\lambda(\tau)$, $\mu(\tau)$), which are responsible for the differences in the three functions (SF(τ; m), ζ(m), and F(τ)) between the inertial and dissipation ranges, are also elucidated in Figure 7.

Supposing that the turbulence amplitude σ has a log-normal distribution, $\lambda(\tau)$ is the standard deviation of the natural logarithm of σ ($\ln(\sigma)$). Again, note that $\lambda(\tau)$ does not increase with decreasing τ, but saturates and even slightly decreases (Alexandrova et al. 2008; Kiyani et al. 2013). This phenomenon may have potential significance for understanding the physical nature of the kinetic range and its essential difference with respect to that of the inertial range. It implies that the dissipation or secondary dispersive cascading, yet to be unambiguously identified, may not only reduce the mean value of $\ln(\sigma)$ but also restrain the growth of the standard deviation of $\ln(\sigma)$. The physical reason for the behavior of $\lambda(\tau)$ in the kinetic range remains an open question for future investigation. Another interesting characteristic is the different break positions of $\mu(\tau)$ and $\lambda(\tau)$: the profiles of $\mu(\tau)$ and $\lambda(\tau)$ turn from one trend to another trend at around 1 s and 7 s, respectively. It remains unknown why the turning of $\lambda(\tau)$ occurs at a larger scale than that of $\mu(\tau)$. Are two relatively independent processes responsible for the different performances of $\lambda(\tau)$ and $\mu(\tau)$?

Although the simplified Castaing function is to some extent a good approximation of PDF(δB(τ)), its symmetry restricts it from being applied to estimating cascading rate, which exists for the asymmetric PDF(δB(τ)). To make a extension, one needs to adopt a more comprehensive Castaing function by introducing some asymmetric factor, e.g., multiplying the symmetric normal distribution (PDF(δB(τ)|σ)) with an asymmetric function defined by a skewness parameter, to resemble the asymmetric PDF(δB(τ)) (Sorriso-Valvo et al. 2015). The scale dependence of the skewness and its relation to the fitting parameters will be investigated in detail in a later work.

The work at Peking University is supported by the National Natural Science Foundation of China (NSFC) under the contracts 41574168, 41874200, 41421003, and 41674171. J.S.H. thank J.-S. Zhao, X. Wang, L.-P. Yang, and L. Zhang for their helpful discussions.

ORCID iDs

Jiansen He https://orcid.org/0000-0001-8179-417X
Luca Sorriso-Valvo https://orcid.org/0000-0002-5981-7758

References

Alexandrova, O., Carbone, V., Veltri, P., & Sorriso-Valvo, L. 2008, ApJ, 674, 1153
Benzi, R., Paladin, G., Parisi, G., et al. 1984, JPhA, 17, 3521
Borovsky, J. E. 2008, JGRA, 113, A08110
Bruno, R., & Carbone, V. 2013, LRSP, 10, 2
Bruno, R., Carbone, V., Veltri, P., et al. 2001, P&SS, 49, 1201
Carbone, V. 1993, PhRvL, 71, 1546
Castaing, B., Gagne, Y., & Hopfinger, E. J. 1990, PhyD, 46, 177
Chandran, B. D., Schekochihin, A. A., & Mallet, A. 2015, ApJ, 807, 39
Frisch, U. 1995, Turbulence: The Legacy of AN Kolmogorov (Cambridge: Cambridge Univ. Press)
Gosling, J. T., Skoug, R. M., McComas, D. J., & Smith, C. W. 2005, GeoRL, 32, L05105
Greco, A., Matthaeus, W. H., Servidio, S., et al. 2009, ApJL, 691, L111
Greco, A., & Perri, S. 2014, ApJ, 784, 163
He, J., Tu, C., Marsch, E., et al. 2015a, ApJL, 813, L30
He, J., Wang, L., Tu, C., et al. 2015b, ApJL, 800, L31
Howes, G. G. 2015, RSPTA, 373, 20140145
Howes, G. G. 2017, PhPl, 24, 055907
Jiansen, H., Xingyu, Z., Yajie, C., et al. 2018, ApJ, 856, 148
Kiyani, K. H., Chapman, S. C., Khotyaintsev, Y. V., et al. 2009, PhRvL, 103, 075006
Kiyani, K. H., Chapman, S. C., Sahraoui, F., et al. 2013, ApJ, 763, 10
Klein, K. G. 2017, PhPl, 24, 055901
Li, G., Miao, B., Hu, Q., et al. 2011, PhRvL, 106, 125001
Liu, Y. H., Drake, J. F., & Swisdak, M. 2012, PhPl, 19, 022110
Luo, Q. Y., Wu, D. J., & Yang, L. 2011, ApJL, 733, L22
Meneveau, C. 1991, JFM, 232, 469
Osman, K. T., Kiyani, K. H., Chapman, S. C., et al. 2014, ApJL, 783, L27
Pei, Z., He, J., Wang, X., Tu, C., et al. 2016, JGRA, 121, 911
Phan, T. D., Gosling, J. T., Davis, M. S., et al. 2006, Natur, 439, 175
Politano, H., & Pouquet, A. 1998, GeoRL, 25, 273
Pulupa, M. P., Salem, C., Phan, T. D., et al. 2014, ApJL, 791, L17
Ragot, B. R. 2013, ApJ, 765, 97
Servidio, S., Greco, A., Matthaeus, W. H., et al. 2011, JGRA, 116, A09102
She, Z. S., & Leveque, E. 1994, PhRvL, 72, 336
Sorriso-Valvo, L., Carbone, F., Perri, S., et al. 2018, SoPh, 293, 10
Sorriso-Valvo, L., Carbone, V., Veltri, P., et al. 1999, GeoRL, 26, 1801
Sorriso-Valvo, L., Marino, R., Lijoi, L., et al. 2015, ApJ, 807, 86
Tu, C. Y., Marsch, E., & Rosenbauer, H. 1996, AnGeo, 14, 270
Wan, M., Matthaeus, W. H., Roytershteyn, V., et al. 2015, PhRvL, 114, 175002
Wang, X., Tu, C., He, J., et al. 2013, ApJL, 772, L14
Wang, Y., Wei, F. S., Feng, X. S., et al. 2015, ApJS, 221, 34
Wu, P., Perri, S., Osman, K., et al. 2013, ApJL, 763, L30
Yang, L., Zhang, L., He, J., et al. 2017, ApJ, 851, 121
Zhang, L., He, J., Tu, C., et al. 2015, ApJL, 804, L43
Zhao, J. S., Voitenko, Y. M., Wu, D. J., et al. 2016, JGRA, 121, 5